Ocean Modelling 192 (2024) 102445

Contents lists available at ScienceDirect

Ocean Modelling

journal homepage: www.elsevier.com/locate/ocemod

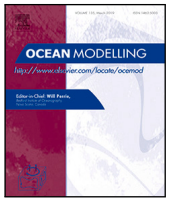

Modeling sediment movement in the shallow-water framework: A morpho-hydrodynamic approach with numerical simulations and experimental validation

E. Guerrero Fernández [a,b,*], M.J. Castro Díaz [c], Y. Wei [a,b], C. Moore [a]

[a] National Oceanic and Atmospheric Administration, Pacific Marine Environmental Laboratory, 7600 Sand Point Way NE Seattle, WA 98115, US
[b] University of Washington, Cooperative Institute for Climate, Ocean and Ecosystem Studies, John M. Wallace Hall, 3737 Brooklyn Ave NE, Seattle, WA 98105, US
[c] Departamento de Análisis Matemático, Faculty of Science, Campus de Teatinos S/N, University of Malaga, 29081 Malaga, Spain

ABSTRACT

This work presents a morpho-hydrodynamic model and a numerical approximation designed for the fast and accurate simulation of sediment movement associated with extreme events, such as tsunamis. The model integrates the well-established hydrostatic shallow-water equations with a transport equation for the moving bathymetry that relies on a bedload transport function. Subsequently, this model is discretized using the path-conservative finite volume framework to yield a numerical scheme that is not only fast but also second-order accurate and well-balanced for the lake-at-rest solution. The numerical discretization separates the hydrodynamic and morphodynamic components of the model but leverages the eigenstructure information to evolve the morphologic part in an upwind fashion, preventing spurious oscillations. The study includes various numerical experiments, incorporating comparisons with laboratory experimental data and field surveys.

1. Introduction

Sediment transport and deposition is a field of great importance in the geophysical sciences. The natural behavior of the sediment bed is of significant importance for the general hydrodynamics of the fluid, especially in shallow areas (see Tang and Weiss, 2016). In general, the literature agrees on splitting the problem into its hydrodynamics and morphodynamical components, that are then coupled through an evolution variable, in general the moving bed function (see Castro Díaz et al., 2008, for instance). This means that the usual challenges that can be found in standard geophysical flow simulations are also present in the case of the sediment transport problem. This includes the great complexity associated with sophisticated models, including non-conservative products terms, or significant numerical challenges when designing accurate and robust numerical schemes.

Sediment transport is often divided in three types: bedload, saltation and suspension. Bedload transport is produced when the sediment rolls or slides along the bed. In saltation transport, the grain jumps over the bed over a total length that is proportional to its diameter. Finally, suspension involves the entrainment of the sediment into the fluid. It is noteworthy that the suspension transport may change the surrounding fluid density significantly, which may in turn increase the total pressure and therefore modify the global hydrodynamic and morphodynamic behavior.

Existing literature for sediment transport includes (Tang and Weiss, 2016; Castro Díaz et al., 2008; Li and Duffy, 2011; Teeter et al., 2001; Castro Díaz et al., 2009; Kurkina et al., 2011). While they all differ in the choice of the sediment flux and/or the numerical treatment of the model, they all agree on the underlying model for the hydrodynamic part of the problem: the shallow-water equations (also known as Saint-Venant equations) (De St Venant, 1871). These equations are derived by vertically averaging the Euler equations such that the vertical component of the velocity is neglected while the horizontal ones are depth-averaged. Although the lack of information in the vertical direction is a potential drawback of this technique, it is counterbalanced by much less computational effort compared to fully three-dimensional models, which is essential for efficient simulations of geophysical flows. Indeed, it reduces the dimension of the problem by one, making it more affordable to simulate large domains with a high horizontal resolution. Adding sediment transport to the shallow-water equations involves the expansion of the original equations with a transport equation for the morphodynamical components that depends on a time-dependent varying bed.

Sediment transport depends heavily on the choice of the model for the solid transport of the sediment flux. These equations are often based on empirical methods and include either deterministic or probabilistic

* Corresponding author at: National Oceanic and Atmospheric Administration, Pacific Marine Environmental Laboratory, 7600 Sand Point Way NE Seattle, WA 98115, US.
E-mail address: ernesto.g.fernandez@noaa.gov (E. Guerrero Fernández).

https://doi.org/10.1016/j.ocemod.2024.102445
Received 13 June 2024; Received in revised form 1 September 2024; Accepted 25 September 2024
Available online 5 October 2024
1463-5003/© 2024 The Authors. Published by Elsevier Ltd. This is an open access article under the CC BY license (http://creativecommons.org/licenses/by/4.0/).

terms. Consequentially, an integral part of the problem resides in the correct choice of the sediment flux equation. Between the existing formulations, we highlight the Grass equation (Grass, 1981), the Meyer-Peter and Müeller's equation (Meyer-Peter and Müller, 1948), Van Rijn's equation (Rijn, 1984,a,b), Nielsen's equation (Nielsen, 1992), Kalinske's equation (Kalinske, 1942, 1947) or Einstein's equation (Zee and Zee, 2017; Einstein, 1950; Julien, 2010; Yalin and Karahan, 1979).

Most physical models and their numerical discretization result from a compromise between physically rich models that are more expensive to resolve compared with simpler, less physical models. This is specially true for sediment transport models. Indeed, these models depend on a correct description of the sediment characteristics, including relative density, friction coefficient, porosity, etc. The difficulty to measure correctly all these parameters constitute an important source of uncertainties. As a consequence, it may be the case that physically complex models yield comparable results to simpler ones, but with much higher computational cost. This effect amplifies when the model is applied in conjunction with large oceanographic phenomena, such as tsunami waves, that have their own sources of uncertainty. For this reason, and since the final goal of this work is to provide a research tool for the NOAA (National Oceanic and Atmospheric Administration) Center for Tsunami Research (NCTR), in this paper we have opted for a simpler set of governing equations.

The resulting set of equations have a set of stationary solutions, or *equilibrium* solutions. These solutions often express a physical reality about the model and its behavior. In this sense, it is very important that any numerical discretization is also able to preserve these solutions. A model that is able to solve stationary solutions exactly is called well-balanced. Otherwise, the numerical noise of a non well-balanced method could significantly alter the final result or even destroy the solution. Therefore, the design of numerical methods must take into account this property, as discussed in Castro Díaz et al. (2008). Other relevant bibliography includes (Audusse et al., 2004; Castro and Parés, 2020; Bermúdez et al., 2017; Canestrelli et al., 2009; Castro Díaz et al., 2007; Guerrero Fernández et al., 2020; Fernández et al., 2021; Guerrero Fernández et al., 2022).

The coupled morpho-hydrodynamic model is a hyperbolic system of conservation laws with non-conservative products and source terms. As discussed in Castro et al. (2006) or Castro et al. (2017), the presence of non-conservative products adds more complexity to the numerical discretization, since its definition in the presence of discontinuities is not unique. In these cases, the non-conservative products can be interpreted as Borel measures (introduced in Dal Maso et al., 1995). In this way, the numerical flux associated with the Riemann problem can be expressed in terms of a free-chosen path linking two states. This is a fundamental result of the path-conservative methods introduced by Parés in Parés (2006).

Furthermore, shallow-water type models with sediment transport present some unique numerical challenges. For instance, in Cordier et al. (2011) the authors prove that splitting techniques that separate the hydrodynamic and morphodynamic part of the model, as is common in the treatment of these kind of systems, may in fact develop spurious oscillations related with a wrong discretization of the flux terms or with a loss of hyperbolicity. Moreover, the authors defend that this unwanted behavior can be avoided by considering a three-wave Riemann solver (in other words, a complete solver for the system) that takes into account the flow of the information associated with the moving bed eigenvalue. Therefore, some authors consider only fully coupled Riemann solvers for these kind of models. Doing so, however, has additional drawbacks. The numerical model is more complex, and the complex eigenstructure of the full model has to be computed at each time step.

To compensate these disadvantages, in this work we propose a novel, weakly-coupled numerical discretization that only uses two waves: an approximation of the maximum and minimum wave speeds. This HLL type numerical discretization evolves the hydrodynamic part independently and then uses this information to evolve the bottom in a upwind fashion. In this way, we avoid increasing the cost of the numerical method while also preventing spurious oscillation like the one discussed in Cordier et al. (2011).

The model presented in this paper is not unique in its ability to simulate sediment transport. Other models, such as SCHISM, MOM6, and Delft3D, offer similar capabilities but with a broader scope. These models are designed as general tools for ocean modeling, covering everything from ocean circulation to tides and biogeochemistry. Some notable differences between these models and the one described in this paper include the use of unstructured mesh simulations, less efficient parallelization with CPU or MPI (Message Passing Interface), the Boussinesq approximation, and the inclusion of vertical effects. It is important to note that not all models share these characteristics, and this list is not exhaustive.

Choosing the appropriate model should then be aligned with the specific problem the user aims to solve. As discussed earlier, incorporating more physical processes does not always lead to greater accuracy due to inherent uncertainties in the source data but it does impact global efficiency and computational times. Moreover, additional physics often require more sophisticated numerical solvers, which can become unstable more easily. To counteract this, many mathematical models and numerical discretizations include a diffusion parameter that must be fine-tuned by the user. However, we completely avoid this approach, as it contradicts our goal of reducing diffusivity by increasing the order of accuracy of the numerical scheme.

In this work we develop a long wave mathematical model that is able to incorporate both, complex hydrodynamics and sophisticated morphodynamics. This combination allows to simulate the sediment behavior associated with extreme flooding events such as tsunamis. Moreover, both the modeling and the numerical method are currently in use at the NCTR, and they are complying with the tools, standards and formats observed at NCTR.

The structure of this article is as follows: in Section 2 we present the governing equations and discuss important aspects of their behavior, including its hyperbolicity. Section 3 presents the novel numerical discretization of the model, including its high order approximation and the two-dimensional extension. Next, Section 4 offers several numerical experiments, including a well-balanced test, an order test and a comparison with laboratory and field data results. Finally, Section 5 gives some conclusions.

2. Model derivation

Let us first consider the shallow-water equations with a moving bed equation. This system consists of a hydrodynamic component that governs the behavior of the fluid, and a morphodynamical component that transports the sediment. Since these equations are well-known in the literature, we will omit a rigorous derivation. The interested reader can refer to Exner (1925) for more details on this. In this way, the two dimensional, $\boldsymbol{x} = (x, y)$, system of partial differential equations evolving in time t reads,

$$\begin{cases} \partial_t h + \nabla_{\boldsymbol{x}} \cdot (h\boldsymbol{u}) = 0, \\ \partial_t (h\boldsymbol{u}) + \nabla_{\boldsymbol{x}} \cdot \left(h\boldsymbol{u} \otimes \boldsymbol{u} + g\dfrac{h^2}{2} \right) = gh\nabla_{\boldsymbol{x}} H - gh\boldsymbol{S}_f, \\ \partial_t H - \nabla_{\boldsymbol{x}} \cdot \boldsymbol{q}_{\boldsymbol{b}} = 0. \end{cases} \tag{1}$$

Here, h is the total water column, $\boldsymbol{u} = (u_x, u_y)$ is the horizontal velocity vector, g stands for the gravity, H is the bathymetry function and $\boldsymbol{S}_f$ represents the friction terms. Of particular interest is $\boldsymbol{q}_{\boldsymbol{b}}$, that controls bedload sediment transport rate per unit time. Finally, $\nabla_{\boldsymbol{x}} = (\partial_x, \partial_y)$ represents the two dimensional spatial derivative operator.

In this way, the partial difference system (1) assumes that the morphodynamical components in the form of sediment transport can be modeled by a transport equation that depends fundamentally on the

sediment flux $\boldsymbol{q_b}$. This transport equation is often denominated as the Exner equation. Note that morphology changes influence the general hydrodynamics of the model by modifying the bathymetry function H, that is present as a source term in the momentum equation.

The system (1) is invariant under rotation if $\boldsymbol{q_b}$ verifies that

$$\boldsymbol{q_b} = |q_b(h, \|\boldsymbol{u}\|)| \frac{\boldsymbol{u}}{\|\boldsymbol{u}\|}, \tag{2}$$

with q_b representing the transport discharge for the sediment in the one-dimensional model. In this way, system (1) is invariant under rotation and we can study, without loss of generality, the simpler, one-dimensional version of system (1) written in non-conservative form:

$$\begin{cases} \partial_t h + \partial_x(hu) = 0, \\ \partial_t(hu) + \partial_x\left(hu^2\right) + gh\partial_x\eta = -ghS_f, \\ \partial_t H - \partial_x q_b = 0. \end{cases} \tag{3}$$

where $\eta = h - H$ is the free surface.

The bedload sediment transport term q_b is responsible for controlling the total sediment movement and behavior. There are many different definitions for this term, most based on empirical descriptions for granular, non-cohesive sediment composition. In the existing literature we can find, among other, the Grass equation (Grass, 1981), the Meyer-Peter and Müeller's equation (Meyer-Peter and Müller, 1948), Van Rijn's equation (Rijn, 1984,a,b), Nielsen's equation (Nielsen, 1992), Kalinske's equation (Kalinske, 1942, 1947) or Einstein's equation (Zee and Zee, 2017; Einstein, 1950; Julien, 2010; Yalin and Karahan, 1979).

These formulations have several common elements. One of them is their dependency of the shear stress with the bottom, defined by:

$$\tau_b = \rho g h S_f. \tag{4}$$

Here, ρ is the fluid density. Note that the shear stress is simply defined by the total weight of the fluid at the bottom times a friction parameter S_f. This friction term is quantified by empirical laws such as Darcy–Weisbach (Darcy, 1857) or Manning (Manning et al., 1890) formula. They are, respectively,

$$S_f = \frac{f u|u|}{8gh}, \tag{5}$$

$$S_f = \frac{n^2 u|u|}{h^{4/3}},$$

where f and n are friction coefficient parameters that depend on the different bathymetry composition and which the user must set appropriately.

It is common to define the bottom shear stress in a dimensionless quantity, θ, known as the Shields parameter. It is defined in terms of the ratio between drag forces and the submerged weight,

$$\theta = \frac{|\tau_b|}{(\rho_s - \rho)g d_s},$$

where ρ_s is the sediment density and d_s is the mean diameter of the sediment.

In fact, the Shields parameter is used to control the threshold value at which the movement starts to takes place. In this way, the Shield parameter θ must exceed some pre-set value θ_{crit} so the motion can take place. This threshold θ_{crit} must be also set by the modeler taking into account the physical properties of the sediment.

Finally, in Castro Díaz et al. (2008) the authors derive a useful general formula for bed transport discharge,

$$q_b = \frac{Q}{1-\phi}\frac{\tau_b}{|\tau_b|} k_1 \theta^{m_1} \left(\theta - \theta_{crit}\right)_+^{m_2} \left(\sqrt{\theta} - \sqrt{\theta_{crit}}\right)_+^{m_3}. \tag{6}$$

In this formula, Q represents the characteristic discharge,

$$Q = \sqrt{\left(\frac{\rho_s}{\rho} - 1\right) g d_s^3},$$

where $(v)_+$ is the positive part of v and ϕ is the porosity of the sediment. Finally, k_1, m_1, m_2 and m_3 are positive real numbers such that

$$k_1 \geq 0, \quad m_1 \geq 0, \quad m_2 \geq 1, \quad m_3 \geq 0.$$

By choosing different values for these coefficients, we can discriminate between different bedload transport formulations. In particular, we have:

- Meyer-Peter and Müller (1948): $k_1 = 8$, $m_1 = 0$, $m_2 = 3/2$ and $m_3 = 0$.
- Luque and Beek (1976): $k_1 = 5.7$, $m_1 = 0$, $m_2 = 3/2$ and $m_3 = 0$.
- Nielsen (1992): $k_1 = 12$, $m_1 = 1/2$, $m_2 = 1$ and $m_3 = 0$.
- Ribberink (1987): $k_1 = 11$, $m_1 = 0$, $m_2 = 1.65$ and $m_3 = 0$.
- Ashida and Michiue (1972): $k_1 = 17$, $m_1 = 0$, $m_2 = 1$ and $m_3 = 1$.

Note that if $k_1 = 0$, then $q_b = 0$, and the transport equation simplifies trivially to $\partial_t H = 0$ and the standard shallow-water equations are recovered.

All these formulas were designed for granular and non-cohesive sediments, mainly for quasi-stationary fluxes in rivers, tides or other phenomena where the time response of the sediment is small compared with fluid velocity. Another limitation of the formulas is given by the exclusion of gradient pressure effect to model grain falling when the velocity of the fluid is zero.

In general, these formulations were designed and benchmarked for a number of applications that are suited for a range of sediment size or channel slope. For instance, for Meyer-Peter and Müller formula, the slopes range from 0.04 to 2%, sediment particle size from 0.4 to 20 mm, flow depth of 0.01 to 1.20 m, water discharge of 0.002 to 2 m^2/s and relative density from 0.25 to 3.2. These data is taken from the comprehensive study of the Meyer-Peter and Müller formula by Hager and Boes in Hager and Boes (2018), and illustrate the difficulty to model sediment transport effects for physical phenomena that are far different from any laboratory setup, such as a tsunami. Therefore, some modifications have to be considered in order to simulate these effects.

2.1. Hyperbolicity

To end this section, let us discuss the hyperbolicity of system (3). In Castro Díaz et al. (2008), the full eigenstructure of system (3) is derived. In particular, it is given by,

$$\begin{aligned} \lambda_1 &= 2\sqrt{S}\, cos(\varphi/3) - a_1/3, \\ \lambda_2 &= 2\sqrt{S}\, cos((\varphi + 2\pi)/3) - a_1/3, \\ \lambda_2 &= 2\sqrt{S}\, cos((\varphi + 4\pi)/3) - a_1/3, \end{aligned} \tag{7}$$

with $S = -(3a_2 - a_1^2)/9$, $\varphi = arcos(R/\sqrt{-S^3})$ and $R = (9a_1a_2 - 27a_3 + 2a_1^3)/54$. Also,

$$a_1 = -2\frac{q}{h}, \qquad a_2 = \frac{q^2}{h^2} - gh\left(1 + \frac{\partial q_b}{\partial q}\right), \qquad a_3 = -gh\frac{\partial q_b}{\partial h},$$

with q being the total flow rate defined by $q = hu$. Note that, if $q_b = 0$, then the bottom is fixed and we recover the well-known shallow-water eigenstructure:

$$\lambda_1 = u + \sqrt{gh}, \qquad \lambda_2 = u - \sqrt{gh}. \tag{8}$$

Furthermore, in Cordier et al. (2011) a thorough discussion about the hyperbolicity of this model can be found. One of their main results was the demonstration that system (3) remains unconditionally hyperbolic if Darcy–Weisbach friction formula (5) is chosen. Unfortunately, the same cannot be said of the Manning friction formula. For this reason, in this work we have chosen to use the Darcy friction formula over that of Manning.

3. Numerical discretization

In this section, we detail the numerical discretization performed to approximate system (3). Our discretization is based on the Finite Volume Method. To make sense of the non-conservative product present in system (1), we make use of the path-conservative framework developed by Parés in Parés (2006).

System (3) can be written in the form of a general hyperbolic system of conservation laws, with conservative fluxes and non-conservative products as follows:

$$\partial \boldsymbol{w} + \partial_x \boldsymbol{F}_C(\boldsymbol{w}) + \boldsymbol{P}(\boldsymbol{w}, \partial_x \eta) = \boldsymbol{S}(\boldsymbol{w}),$$

where $\boldsymbol{w}$ is the state vector of conserved variables defined by:

$$\boldsymbol{w} = (h, hu, H)^T.$$

Likewise, the conservative flux $\boldsymbol{F}_C$ is given by:

$$\boldsymbol{F}_C = \left(hu, hu^2, -q_b\right)^T,$$

while the pressure term $\boldsymbol{P}$ and the source term $\boldsymbol{S}$ are given by the following expressions respectively,

$$\boldsymbol{P} = (0, gh\partial_x \eta, 0)^T,$$

$$\boldsymbol{S} = (0, -gh\, S_f, 0)^T.$$

As commented before, the bottom friction S_f is given by the Darcy–Weisbach formula (5).

Since the friction term will be taken into account at a later point, the actual system we solve at this stage is given by:

$$\partial \boldsymbol{w} + \partial_x \boldsymbol{F}_C(\boldsymbol{w}) + \boldsymbol{P}(\boldsymbol{w}, \partial_x \eta) = \boldsymbol{0}.$$

We will now derive the second-order accurate path-conservative finite volume method, based on a hydrostatic reconstruction technique and able to preserve lake-at-rest type stationary solutions.

Let us consider a uniform grid discretization of the computational domain Ω in cells $\Omega_i = [x_{i-\frac{1}{2}}, x_{i+\frac{1}{2}}]$ of a constant length $\Delta x = x_{i+\frac{1}{2}} - x_{i-\frac{1}{2}}$. As usual, the approximation of the solution at time $t^n = n\Delta t$ is averaged across the cell, and denoted by $\boldsymbol{w}_i^n$,

$$\boldsymbol{w}_i^n \approx \frac{1}{\Delta x} \int_{x_{i-\frac{1}{2}}}^{x_{i+\frac{1}{2}}} \boldsymbol{w}(x, t^n)\, dx.$$

Additionally, from now on we will denote the cell average at the cell interface for any variable f as

$$\bar{f} \equiv \bar{f}_{i+\frac{1}{2}} = \frac{1}{2}(f_i + f_{i+1}). \tag{9}$$

Likewise, the difference at the intercell is denoted as,

$$\Delta f \equiv \Delta f_{i+\frac{1}{2}} = f_{i+1} - f_i \tag{10}$$

3.1. First order HLL scheme

As discussed in the introduction, a careless numerical discretization that address the hydrodynamic and morphodynamic part separately can develop spurious oscillations. This is the reason why some authors consider complete Riemann solvers for the system (3). However, doing so forces the computation of the full eigenstructure (7) at each time step, introducing a significant computational overhead.

To address these drawbacks, our approach introduces a weakly coupled numerical discretization that employs only two waves, representing approximations of the maximum and minimum wave speeds (8). This HLL-type numerical discretization independently evolves the hydrodynamic component and subsequently utilizes this information to evolve the bottom in an upwind fashion.

For the description of the numerical discretization we distinguish between the hydrostatic and the morphological part. We use $(f)_{[h,hu]}$ when variable f refers to the hydrostatic part, corresponding to the mass and momentum equations in system (3). Following Castro and Fernández-Nieto (2012), we define a Polynomial Viscosity Matrix (PVM) HLL-type scheme for the hydrostatic part of (3) by

$$(\boldsymbol{w}_i^{n+1})_{[h,hu]} = (\boldsymbol{w}_i^n)_{[h,hu]} - \frac{\Delta t}{\Delta x}\left((\boldsymbol{D}^+_{i-\frac{1}{2}}(\boldsymbol{w}_{i-1}^n, \boldsymbol{w}_i^n))_{[h,hu]} + (\boldsymbol{D}^-_{i+\frac{1}{2}}(\boldsymbol{w}_i^n, \boldsymbol{w}_{i+1}^n))_{[h,hu]}\right), \tag{11}$$

where $(\boldsymbol{D}^{\mp}_{i\pm\frac{1}{2}})_{[h,hu]}$, the numerical fluxes, are defined by,

$$(\boldsymbol{D}^-_{i+\frac{1}{2}})_{[h,hu]} = \frac{1}{2}\left((1-\alpha_{1,i+\frac{1}{2}})\boldsymbol{E}_{i+\frac{1}{2}} - \alpha_{0,i+\frac{1}{2}}((\boldsymbol{w}_{i+1})_{[h,hu]} - (\boldsymbol{w}_i)_{[h,hu]})\right) + (\boldsymbol{F}_C(\boldsymbol{w}_i))_{[h,hu]}, \tag{12}$$

$$(\boldsymbol{D}^+_{i+\frac{1}{2}})_{[h,hu]} = \frac{1}{2}\left((1+\alpha_{1,i+\frac{1}{2}})\boldsymbol{E}_{i+\frac{1}{2}} + \alpha_{0,i+\frac{1}{2}}((\boldsymbol{w}_{i+1})_{[h,hu]} - (\boldsymbol{w}_i)_{[h,hu]})\right) - (\boldsymbol{F}_C(\boldsymbol{w}_{i+1}))_{[h,hu]}, \tag{13}$$

and

$$\boldsymbol{E}_{i+\frac{1}{2}} = (\boldsymbol{F}_C(\boldsymbol{w}_{i+1}))_{[h,hu]} - (\boldsymbol{F}_C(\boldsymbol{w}_i))_{[h,hu]} + (\boldsymbol{P}_{i+\frac{1}{2}})_{[h,hu]}. \tag{14}$$

$(\boldsymbol{P}_{i+\frac{1}{2}})_{[h,hu]}$ is a simple discretization of the pressure terms, given by

$$(\boldsymbol{P}_{i+\frac{1}{2}})_{[h,hu]} = (0, g\bar{h}\Delta\eta)^T.$$

Using (9) and (10), a full version of the pressure terms are given by,

$$(\boldsymbol{P}_{i+\frac{1}{2}})_{[h,hu]} = \left(0, g\frac{1}{2}(h_i + h_{i+1})(\eta_{i+1} - \eta_i)\right)^T. \tag{15}$$

Note that by discretizing the free surface term instead of the water depth, we are able to preserve stationary solutions corresponding with constant free surface, $\eta = cst$.

The coefficients $\alpha_{0,i+\frac{1}{2}}$ and $\alpha_{1,i+\frac{1}{2}}$ are related with the viscosity of the scheme. According to Castro and Fernández-Nieto (2012), for the HLL scheme these coefficients take the following form,

$$\alpha_{0,i+\frac{1}{2}} = \frac{\lambda^+_{i+\frac{1}{2}}|\lambda^-_{i+\frac{1}{2}}| - \lambda^-_{i+\frac{1}{2}}|\lambda^+_{i+\frac{1}{2}}|}{\lambda^+_{i+\frac{1}{2}} - \lambda^-_{i+\frac{1}{2}}}, \qquad \alpha_{1,i+\frac{1}{2}} = \frac{|\lambda^+_{i+\frac{1}{2}}| - |\lambda^-_{i+\frac{1}{2}}|}{\lambda^+_{i+\frac{1}{2}} - \lambda^-_{i+\frac{1}{2}}}, \tag{16}$$

where $\lambda^{\pm}_{i+\frac{1}{2}}$ are an approximation of the minimum and maximum wave speeds. Note that in those coefficients the influence of the sediment layer should be considered. Nevertheless, we propose to use the shallow-water eigenvalues (8),

$$\lambda^{\pm}_{i+\frac{1}{2}} = \bar{u} \pm \sqrt{g\bar{h}}. \tag{17}$$

Remark 1. As discussed in Section 2.1, eigenvalues (17) are not the eigenvalues of the full system (3), which are given by (7). But in this work we propose to use (17) as an approximation to wave speed, since it is easier and faster to evaluate. In the following paragraphs we will discuss how to apply this approximations to evolve the morphological part of system (3) in a weakly-coupled fashion without instabilities.

This completes the description of the first order numerical scheme for the hydrodynamic part of (3). In order to evolve the morphodynamical part, an upwind scheme is used in the morphodynamical component. In the oncoming description of the morphodynamical scheme we denote by $(f)_{[H]}$ when variable f refers to the morphological part, corresponding to the bedload transport equation in system (3). Then, the following numerical scheme for the morphological part of (3) is proposed:

$$(\boldsymbol{w}_i^{n+1})_{[H]} = (\boldsymbol{w}_i^n)_{[H]} - \frac{\Delta t}{\Delta x}\left((\boldsymbol{D}^+_{i-\frac{1}{2}}(\boldsymbol{w}_{i-1}^n, \boldsymbol{w}_i^n))_{[H]} + (\boldsymbol{D}^-_{i+\frac{1}{2}}(\boldsymbol{w}_i^n, \boldsymbol{w}_{i+1}^n))_{[H]}\right). \tag{18}$$

On this occasion, $(\boldsymbol{D}^{\mp}_{i\pm\frac{1}{2}})_{[H]}$, the numerical fluxes, are defined by,

$$(\boldsymbol{D}^{-}_{i+\frac{1}{2}})_{[H]} = \frac{1}{2}(1-\beta_{i+\frac{1}{2}})\boldsymbol{E}_{i+\frac{1}{2}} + (\boldsymbol{F}_C(\boldsymbol{w}_i))_{[H]}, \tag{19}$$

$$(\boldsymbol{D}^{+}_{i+\frac{1}{2}})_{[H]} = \frac{1}{2}(1+\beta_{i+\frac{1}{2}})\boldsymbol{E}_{i+\frac{1}{2}} - (\boldsymbol{F}_C(\boldsymbol{w}_{i+1}))_{[H]}, \tag{20}$$

and

$$\boldsymbol{E}_{i+\frac{1}{2}} = (\boldsymbol{F}_C(\boldsymbol{w}_{i+1}))_{[H]} - (\boldsymbol{F}_C(\boldsymbol{w}_i))_{[H]}. \tag{21}$$

Here, $\beta_{i+\frac{1}{2}}$ is given by

$$\beta_{i+\frac{1}{2}} = \begin{cases} \alpha_{1,i+\frac{1}{2}} & \text{if } sgn(\alpha_{1,i+\frac{1}{2}}) = \frac{sgn(F_C((\boldsymbol{w}_{i+1})_{[H]}) - F_C((\boldsymbol{w}_i)_{[H]}))}{sgn(H_{i+1}-H_i)}, \\ -\alpha_{1,i+\frac{1}{2}} & \text{otherwise.} \end{cases} \tag{22}$$

In this way, the morphodynamical part of (3) is evolved using the wave speed information of the hydrodynamic part but taking into account if the hydrodynamics's flux direction is the same as the morphodynamical one. Note that if the physical flux difference of the hydrodynamic part of the scheme has the same sign (i.e. the same direction) that the flux difference of the morphological part, then we use $\alpha_{1,i+\frac{1}{2}}$ to evolve the morphological part. Note that $\alpha_{1,i+\frac{1}{2}}$ comes from the hydrodynamic part.

Remark 2. Under the PVM theory, the numerical scheme (18)–(22) is not exactly the HLL scheme. In fact, this scheme could be seen as a modification of the HLL scheme for the complete system, where the hydrodynamical component is discretized using the HLL scheme and the morphodynamical one is treated like an upwind-type discretization using the information of the hydrodynamical component ($\alpha_{1,i+1/2}$), but with the sign of the approximation of the wave speed for the morphodynamical component, that ensures the stability of the proposed scheme.

Remark 3. In the case of flat bathymetry in (22), then only the conservative flux is considered, i.e,

$$\beta_{i+\frac{1}{2}} = \begin{cases} \alpha_{1,i+\frac{1}{2}} & \text{if } sgn(\alpha_{1,i+\frac{1}{2}}) = sgn(F_C((\boldsymbol{w}_{i+1})_{[H]}) - F_C((\boldsymbol{w}_i)_{[H]})), \\ -\alpha_{1,i+\frac{1}{2}} & \text{otherwise.} \end{cases}$$

The final solution $\boldsymbol{w}_i^{n+1}$ results from the concatenation of the hydrodynamic and morphodynamic parts,

$$\boldsymbol{w}_i^{n+1} = \left[(\boldsymbol{w}_i^{n+1})_{[h,hu]}, (\boldsymbol{w}_i^{n+1})_{[H]}\right]^T.$$

Likewise, the final numerical scheme concatenates numerical fluxes as well, resulting in the following expression,

$$\boldsymbol{w}_i^{n+1} = \boldsymbol{w}_i^n - \frac{\Delta t}{\Delta x}\left(\boldsymbol{D}^{+}_{i-\frac{1}{2}}(\boldsymbol{w}_{i-1}^n, \boldsymbol{w}_i^n) + \boldsymbol{D}^{-}_{i+\frac{1}{2}}(\boldsymbol{w}_i^n, \boldsymbol{w}_{i+1}^n)\right), \tag{23}$$

with

$$\boldsymbol{D}^{+}_{i-\frac{1}{2}}(\boldsymbol{w}_{i-1}^n, \boldsymbol{w}_i^n) = \left[(\boldsymbol{D}^{+}_{i-\frac{1}{2}}(\boldsymbol{w}_{i-1}^n, \boldsymbol{w}_i^n))_{[h,hu]}, (\boldsymbol{D}^{+}_{i-\frac{1}{2}}(\boldsymbol{w}_{i-1}^n, \boldsymbol{w}_i^n))_{[H]}\right]^T, \tag{24}$$

$$\boldsymbol{D}^{-}_{i+\frac{1}{2}}(\boldsymbol{w}_i^n, \boldsymbol{w}_{i+1}^n) = \left[(\boldsymbol{D}^{-}_{i+\frac{1}{2}}(\boldsymbol{w}_i^n, \boldsymbol{w}_{i+1}^n))_{[h,hu]}, (\boldsymbol{D}^{-}_{i+\frac{1}{2}}(\boldsymbol{w}_i^n, \boldsymbol{w}_{i+1}^n))_{[H]}\right]^T. \tag{25}$$

3.2. Hydrostatic reconstruction

In this section, we describe the hydrostatic reconstruction technique (Audusse et al., 2004; Castro et al., 2007) applied to the numerical scheme (23). Given two states $\boldsymbol{w}_{i+1}$ and $\boldsymbol{w}_i$, we defined two reconstructed states for the Riemann solver at the cell interfaces $\boldsymbol{w}^{\pm}_{i+\frac{1}{2}}$ in the following way:

$$H^{HR}_{i+\frac{1}{2}} = min(H_i, H_{i+1}) \tag{26}$$

and

$$h^{HR,-}_{i+\frac{1}{2}} = \left(h_i^n - H_i + H^{HR}_{i+\frac{1}{2}}\right)_+, \qquad h^{HR,+}_{i+\frac{1}{2}} = \left(h_{i+1}^n - H_{i+1} + H^{HR}_{i+\frac{1}{2}}\right)_+. \tag{27}$$

Here $(f)_+$ denotes the positive part of f. Using (27) we define the new state values as:

$$\boldsymbol{w}^{HR,\pm}_{i+\frac{1}{2}} = \left(h^{HR,\pm}_{i+\frac{1}{2}}, h^{HR,\pm}_{i+\frac{1}{2}}u, H^{HR}_{i+\frac{1}{2}}\right)^T. \tag{28}$$

Note that u remains unchanged, that is, the velocity is the one corresponding to the original state.

Observe that the states defined at the cell interface (9)–(10) are now defined in terms of the hydrostatic reconstructed states (28). The first order HLL numerical scheme (23) now reads,

$$\boldsymbol{w}_i^{n+1} = \boldsymbol{w}_i^n - \frac{\Delta t}{\Delta x}\left(\boldsymbol{D}^{+}_{i-\frac{1}{2}}(\boldsymbol{w}^{HR,-}_{i-\frac{1}{2}}, \boldsymbol{w}^{HR,+}_{i-\frac{1}{2}}) + \boldsymbol{D}^{-}_{i+\frac{1}{2}}(\boldsymbol{w}^{HR,-}_{i+\frac{1}{2}}, \boldsymbol{w}^{HR,+}_{i+\frac{1}{2}})\right). \tag{29}$$

The definition of the numerical fluxes (24)–(25) remains the same but, since the hydrostatic reconstruction keeps the bottom variable constant, the pressure terms is now simplified as follows:

$$\boldsymbol{P}_{i+\frac{1}{2}} = (0, g\bar{h}\Delta h, 0)^T.$$

Remark 4. In the generalized hydrostatic reconstruction presented in Castro et al. (2007), the numerical scheme (29) should include a correction due to the hydrostatic reconstruction that guarantees the consistency of the scheme. This term arises from the evaluation of the integral of the pressure terms along the path that links the cell states at the center with their hydrostatic reconstructed counterparts (28). However, since the hydrostatic reconstruction within a cell keeps the free surface constant, this evaluation is zero (29).

Corollary 5. *The resulting numerical scheme (29) is positive preserving for the total water column h under the standard CFL-1/2 condition, since the hydrostatic reconstruction maintains this well-known property of the HLL numerical schemes (see Audusse et al., 2004, for instance). Additionally, the scheme is able to preserve stationary solutions corresponding to constant total free surface and zero velocity.*

Remark 6. As already mentioned, in order for the scheme to ensure positivity, the CFL condition must be CFL ≤ 0.5.

3.3. Second order extension

So far, the numerical scheme (29) is first order in space and time. As proved in Cordier et al. (2011), low diffusion schemes are essential to capture complex morphodynamical behaviors. To reach second order in space, we define a reconstruction operator that provides a second order approximation of the state values $\boldsymbol{w}_i^n$. In this way, at each cell Ω_i and at each time t^n, we define the reconstruction function $\boldsymbol{R}_i^t(x) = \boldsymbol{w}(x,t) + \mathcal{O}(\Delta x^2)$, $\forall\, x \in \Omega_i$. In order to define $\boldsymbol{R}_i^t(x)$, both the cell value $\boldsymbol{w}_i^n$ and its immediate neighbors are used. Additionally, we will use the standard notation for reconstruction operators:

$$\lim_{x\to x^+_{i-\frac{1}{2}}} \boldsymbol{R}_i^t(x) = \boldsymbol{w}^+_{i-\frac{1}{2}}(t), \qquad \lim_{x\to x^-_{i+\frac{1}{2}}} \boldsymbol{R}_i^t(x) = \boldsymbol{w}^-_{i+\frac{1}{2}}(t). \tag{30}$$

In Castro et al. (2017), it was shown that the semidiscrete extension of the first order numerical scheme (29) is:

$$\boldsymbol{w}_i'(t) = -\frac{1}{\Delta x}\left(\boldsymbol{D}^{+}_{i-\frac{1}{2}}(t) + \boldsymbol{D}^{-}_{i+\frac{1}{2}}(t)\right) - \frac{1}{\Delta x}\int_{x_{i-\frac{1}{2}}}^{x_{i+\frac{1}{2}}} \boldsymbol{P}(\boldsymbol{R}_i^t, \partial_x R_i^{\eta,t})\, dx. \tag{31}$$

Here, $R_i^{\eta,t}$ denotes the reconstruction operator applied to the free surface η. In general, we denote $R_i^{f,t}$ as the reconstruction of the variable

f. In this way, the components of $\boldsymbol{R}_i^t$ are $\boldsymbol{R}_i^t = (R^h, R^{hu}, R^H)$. Note that the numerical fluxes $\boldsymbol{D}^{\mp}_{i\pm\frac{1}{2}}$ are computed using the reconstructed states:

$$\boldsymbol{D}^+_{i-\frac{1}{2}}(t) = \boldsymbol{D}^+_{i-\frac{1}{2}}(t)(\boldsymbol{w}^-_{i-\frac{1}{2}}(t), \boldsymbol{w}^+_{i-\frac{1}{2}}(t)),$$

$$\boldsymbol{D}^-_{i+\frac{1}{2}}(t) = \boldsymbol{D}^-_{i+\frac{1}{2}}(t)(\boldsymbol{w}^-_{i+\frac{1}{2}}(t), \boldsymbol{w}^+_{i+\frac{1}{2}}(t)).$$

Remark 7. The hydrostatic reconstruction presented in Section 3.2 is applied using the second order approximation of the states (30). In this way, the hydrostatic reconstructed states (26)–(27) now reads:

$$H^{HR}_{i+\frac{1}{2}} = min(H^-_{i+\frac{1}{2}}, H^+_{i+\frac{1}{2}})$$

and

$$h^{HR,-}_{i+\frac{1}{2}} = \left(h^-_{i+\frac{1}{2}} - H^-_{i+\frac{1}{2}} + H^{HR}_{i+\frac{1}{2}}\right)_+,$$
$$h^{HR,+}_{i+\frac{1}{2}} = \left(h^n_{i+1} - H_{i+1} + H^{HR}_{i+\frac{1}{2}}\right)_+.$$

As it was discussed in Castro et al. (2017), to preserve the global well-balanced property of the first order numerical scheme (29), the reconstruction operators must also be well-balanced. This means that the reconstruction operator should provide the exact value when encountering the kind of stationary solution that we are interested in preserving, i.e., the lake-at-rest type of stationary solutions:

$$R^\eta_i = R^h_i - R^H_i = cst. \tag{32}$$

To achieve this, the well-known procedure include reconstructing the free surface η and the total water depth h, and obtaining the bathymetry reconstruction as a subproduct of (32),

$$R^H_i = R^h_i - R^\eta_i.$$

The reason why this procedure preserves the lake-at-rest stationary solution is because the reconstruction operator depends on the first order approximation of the derivative of the solution at the cell interfaces, which are exact for the constant operator.

In particular, for this work we will use the MUSCL reconstruction operator (Leer, 1979). In this way, the reconstruction operator $\boldsymbol{R}_i^t$ is defined as follows:

$$\boldsymbol{R}^t_i(x) = \boldsymbol{w}_i + \boldsymbol{\sigma}(x - x_i). \tag{33}$$

Here, $\boldsymbol{\sigma}_i$ denotes the slope of the reconstruction for each variable and x_i is the center of the cell Ω_i. As usual, some kind of slope limiter is necessary in order to prevent spurious oscillation near strong gradients or discontinuities. To achieve this, we consider an average limiter (avg), defined by

$$avg(a,b) = \begin{cases} \frac{|a|b+a|b|}{|a|+|b|} & |a|+|b| > 0, \\ 0 & \text{otherwise.} \end{cases}$$

Using this average limiter, the slope for the kth component of the vector is defined by,

$$[\boldsymbol{\sigma}_i]_k = avg\left(\frac{[\boldsymbol{w}_{i+1} - \boldsymbol{w}_i]_k}{\Delta x}, \frac{[\boldsymbol{w}_i - \boldsymbol{w}_{i-1}]_k}{\Delta x}\right).$$

In this way, we can summarize the reconstruction procedure as follows:

- In the first place, the total water depth h and the free surface η are reconstructed and then the bathymetry variable H is recovered with $R^H_i = R^h_i - R^\eta_i$.
- Secondly, the primitive variable u is reconstructed using $R^u_i(x) = u_i + \sigma^u(x - x_i)$. The high order approximation of the conservation variable hu is performed taking into account the following,

$$\sigma^{hu}_i = \partial_x R^{hu}_i = R^h_i(x_i)\partial_x R^u_i + R^u_i(x_i)\partial_x R^h_i$$

Next, the integral term in (31) can be approximated by a middle point quadrature rule,

$$\frac{1}{\Delta x}\int_{x_{i-\frac{1}{2}}}^{x_{i+\frac{1}{2}}} \boldsymbol{P}(\boldsymbol{R}^t_i, \partial_x R^{\eta,t}_i)\, dx \approx \boldsymbol{P}_i.$$

Note that, since the middle point rule is a second-order approximation of the integral operator, it preserves the total order of accuracy of the scheme.

Finally, the second order in time is achieved using to a total variation diminish (TVD) Runge–Kutta method (see Gottlieb and Shu, 1996).

The numerical scheme thus defined is second-order accurate in space and time. Additionally, it is able to preserve stationary solutions corresponding to constant water surface and it is positive preserving with a suitable CFL condition.

3.4. Friction terms

As already discussed, the friction term is split and taken into account at a later stage. For the case of the first order numerical scheme, the numerical solution described in Sections 3.1 to 3.3 is now renamed from $\boldsymbol{w}_i^{n+1}$ to $\boldsymbol{w}_i^{n+1/2}$. Next, the final solution at time t^{n+1} is given by the following semi-implicit update:

$$\boldsymbol{w}_i^{n+1} = \boldsymbol{w}_i^{n+1/2} + \Delta t \boldsymbol{S}(\boldsymbol{w}_i^n, \boldsymbol{w}_i^{n+1}),$$

with

$$\boldsymbol{S}(\boldsymbol{w}_i^n, \boldsymbol{w}_i^{n+1}) = (0, -\frac{f q_i^{n+1}}{8h_i^{n+1}}|u_i^n|, 0)$$

for the Darcy friction law. Note that this update is performed for both stages of the Runge–Kutta method when the second order approach is used.

Finally, we can see a flow chart of the complete numerical approach in Fig. 1.

3.5. Two-dimensional extension

In this subsection, we will discuss the two dimensional extension of the shallow-water system (3) and the numerical scheme discussed so far in this section. The two-dimensional set of equations was previously written in (1). We can write this system using its vector components $\boldsymbol{x} = (x, y)$ as follows,

$$\begin{cases} \partial_t h + \partial_x(hu_x) + \partial_y(hu_y) = 0, \\ \partial_t(hu_x) + \partial_x\left(hu_x^2\right) + \partial_y(hu_x u_y) + gh\partial_x\eta = -ghS_{x,f}, \\ \partial_t(hu_x) + \partial_y\left(hu_y^2\right) + \partial_x(hu_y u_x) + gh\partial_y\eta = -ghS_{y,f}, \\ \partial_t H - \partial_x q_{x,b} - \partial_y q_{y,b} = 0. \end{cases} \tag{34}$$

Here, $q_{x,b}$ and $q_{y,b}$ are defined using (2),

$$q_{x,b} = \left|q_b(h, \|\boldsymbol{u}\|)\right| \frac{u_x}{\|\boldsymbol{u}\|}, \qquad q_{y,b} = \left|q_b(h, \|\boldsymbol{u}\|)\right| \frac{u_y}{\|\boldsymbol{u}\|}.$$

The PDE system (34) can be written in the compact form,

$$\partial\boldsymbol{w} + \partial_x \boldsymbol{F}_C(\boldsymbol{w}) + \partial_y \boldsymbol{G}_C(\boldsymbol{w}) + \boldsymbol{P}_x(\boldsymbol{w}, \partial_x\eta) + \boldsymbol{P}_y(\boldsymbol{w}, \partial_y\eta) = \boldsymbol{S}_x(\boldsymbol{w}) + \boldsymbol{S}_y(\boldsymbol{w}).$$

In this occasion, the new state variables are,

$$\boldsymbol{w} = \left(h, hu_x, hu_y, H\right)^T,$$

while the physical fluxes are given by,

$$\boldsymbol{F}_C(\boldsymbol{w}) = \left(hu_x, hu_x^2, hu_y u_x, q_{x,b}\right), \qquad \boldsymbol{G}_C(\boldsymbol{w}) = \left(hu_y, hu_y^2, hu_x u_y, q_{y,b}\right).$$

Likewise, the pressure terms are defined as follows,

$$\boldsymbol{P}_x(\boldsymbol{w}, \partial_x\eta) = (0, gh\partial_x\eta, 0, 0), \qquad \boldsymbol{P}_y(\boldsymbol{w}, \partial_y\eta) = (0, 0, gh\partial_y\eta, 0).$$

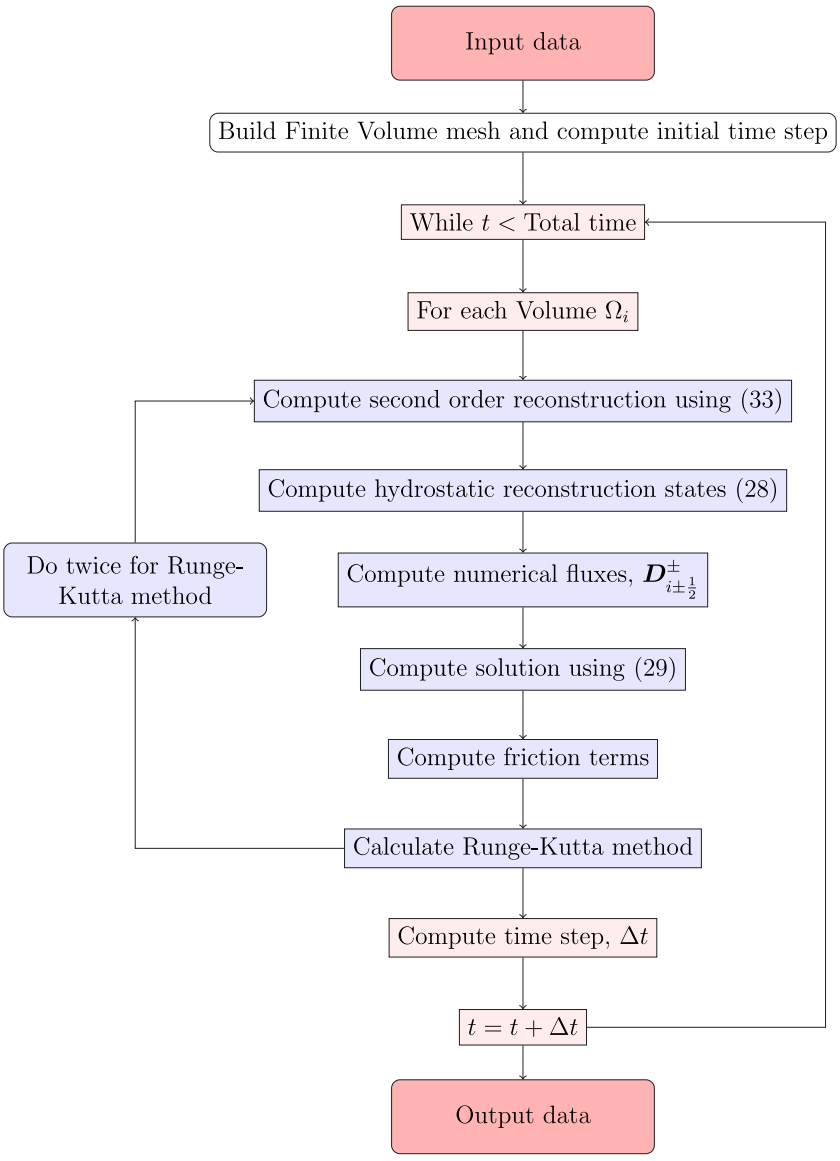

Fig. 1. Flow chart of the numerical approach.

Finally, the friction terms are defined in a similar fashion,

$$\boldsymbol{S}_x(\boldsymbol{w}) = (0, ghS_{x,f}, 0, 0), \qquad \boldsymbol{S}_y(\boldsymbol{w}) = (0, 0, ghS_{y,f}, 0).$$

Note that system (34) can be written in a dimension-by-dimension fashion, resulting in the same one dimensional system (3) with the addition of a transport equation. Therefore, the same numerical scheme can be applied and the numerical properties are kept intact. The interested reader can refer to De la Asunción et al. (2013) for more details.

4. Numerical results and discussions

In this section, we perform several numerical simulations in order to show the capacity and the global accuracy of the model. A total of six different experiments are considered. The first experiment is an order test to show that we reach the desired convergence order of accuracy. Additionally, a well-balanced test is also included. We also consider two laboratory experiments where empirical data is available for comparison purposes. The final two simulations include comparisons of the sediment distribution after the 2011 Tōhoku tsunami event, both for Crescent City harbor (California, U.S.) and for Hirota Bay (Rikuzentakata City, Japan). In general, the comparisons show excellent data agreement between the empirical data and the numerical simulations.

For all tests in this section, the CFL condition is set to 0.9 and, unless stated otherwise, we use Meyer-Peter and Müller formula for the transport discharge (6).

4.1. Order test

The first test seeks to prove numerically the global order of accuracy of the numerical scheme. In order to do that, we consider a one dimensional simulation with an increasing grid discretization of 50, 100, 200 and 400 points, that are compared with a reference solution computed with 4800 discretization points. The simulation domain is given by $\Omega = [-5, 5]$. The initial condition is given by the following free surface and bathymetry function:

$$\eta = 1 + \frac{1}{10} e^{-5x^2}, \qquad H = -\frac{1}{2} e^{-5x^2}.$$

Likewise, the ratio of density for the sediment is 2.7 kg/cm^3, the mean diameter of sediment grain is 0.2 mm, the friction coefficient $f = 0.01$ while the porosity is $\phi = 0.43$ and $\theta_{crit} = 0.047$.

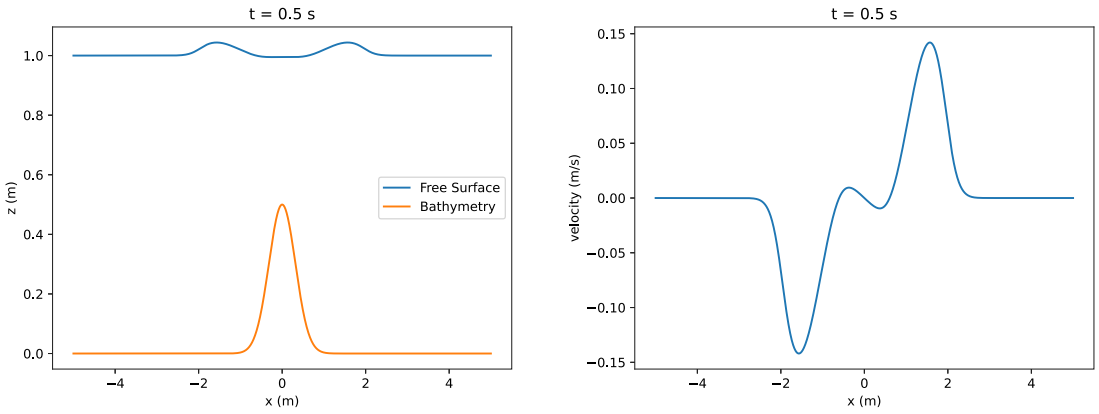

Fig. 2. Free surface and bathymetry (**left**) and velocities (**right**) at time $t = 0.5$ s for the second order scheme.

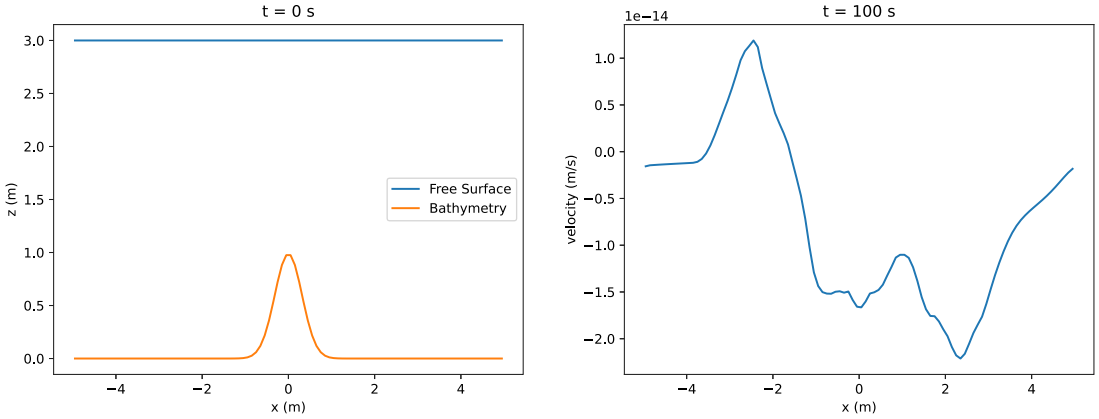

Fig. 3. Cut at the plane $x = 0$ depicting the free surface and bathymetry initial condition (**left**) and velocities at time $t = 100$ s (**right**).

Table 1
Order of accuracy for the second order scheme.

N. cells	h		hu		H	
	Error	Order	Error	Order	Error	Order
50	2.22e−02	–	5.23e−02	–	6.09e−03	–
100	6.29e−03	1.82	1.56e−02	1.75	1.61e−03	1.92
200	1.56e−03	2.02	3.97e−03	1.97	4.00e−04	2.01
400	4.41e−04	1.82	9.90e−04	2.00	1.02e−04	1.97

The simulation is computed for a total of $t = 0.5$ s, with periodic boundary conditions everywhere. Fig. 2 shows the simulation at final time for the reference solution. The results can be consulted in Table 1, where the error with respect to the reference solution and the global order of accuracy is displayed for all conserved variables. As we can see, the desired order of convergence is achieved.

4.2. Well-balanced test

For the well-balanced test, we set a stationary solution and ensure that it remains constant as it evolves with time. In particular, the initial condition is given by,

$$\eta = 3 \qquad H = -e^{-5x^2}.$$

This initial condition can be seen in Fig. 3 (left).

The computational domain $\Omega = [-5,5] \times [-5,5]$ is divided with 100×100 discretization points and the total simulated time is $t = 100$ s. We can see that the at the free surface remains constant and the velocities are zero up to machine precision (see Fig. 3, right). Again, periodic boundary conditions are set.

4.3. Laboratory experiment with dune and no slope

This test focuses on replicating the results of the morphology of a test where laboratory data is available. As already discussed, Yoshii et al. presented in Yoshii et al. (2017, 2018) a number of laboratory experiments where different wave profiles were tested for several morphological distributions. These experiments are undertaken in a wave-flume 205 m long and 3.4 m wide, with an uniformly sloping topography (1/50) with a sand dune 0.2 m high. After the dune, the topography becomes flat (see Fig. 4, left). Next, a wave designed to simulate a tsunami is produced at the beginning of the channel, and the water height and velocity are measured every 0.01 s as well as topography change before and after the event. The data is offered at two different locations and we use it directly as boundary conditions at the location right before the dune. We remark that this data is publicly available and we forward the interested readers to Yoshii et al. (2017, 2018) and supplementary materials therein. The data provided includes free surface evolution, sediment composition and final morphological distribution. For this test, denominated test C11 in Yoshii et al. (2018), the authors set the following sediment distribution: sediment size of 0.12 mm and relative density of the sediment of 2.84. Additionally, we set the Darcy–Weisbach friction coefficient to $f = 4 \times 10^{-2}$, porosity to $\phi = \frac{1}{2}$ and $\theta_{crit} = 0.047$.

The problem is discretized in one dimension using 500 elements, and it is run for 130 s. Note that these experiments are inherently one dimensional, in order to minimize uncertainty of sources. Therefore, we perform one-dimensional simulations as well. For the boundary conditions, we simply impose the measurements provided in Yoshii et al. (2018) thorough Dirichlet boundary conditions. These are a

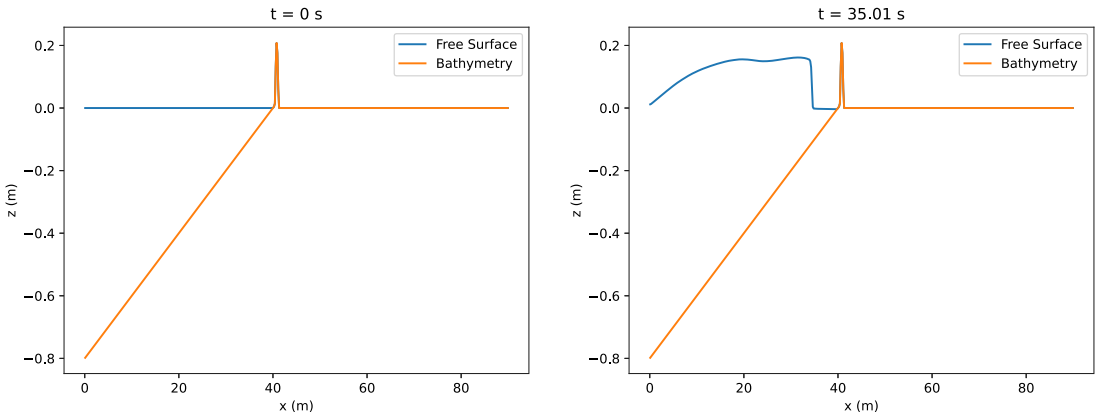

Fig. 4. Initial free surface and bathymetry (**left**) and free surface and bathymetry at time $t = 35$ s (**right**).

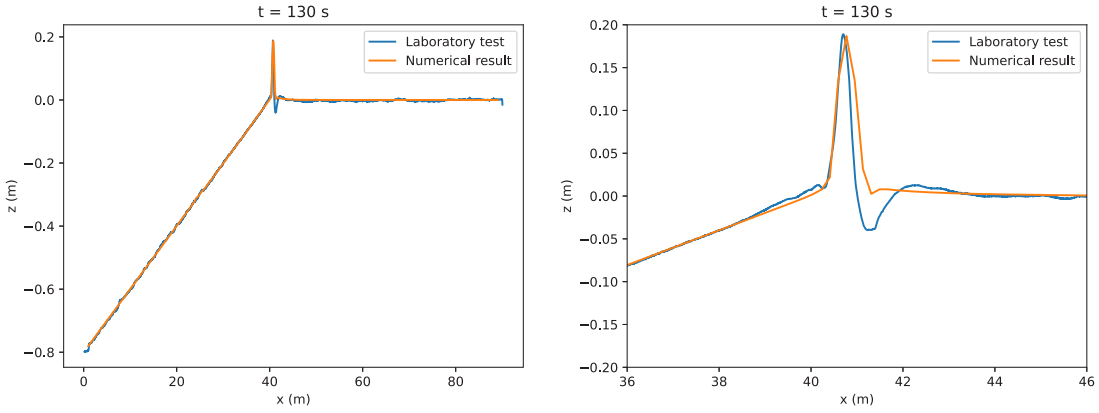

Fig. 5. Laboratory and numerical bathymetry distribution at final time $t = 130$ s (**left**) and zoom (**right**).

well-known technique in the finite volume framework, and the interested reader can refer to Toro (2013) for more details on applying them. Fig. 4 (left) shows the initial condition for the free surface and bathymetry. The final results for the morphodynamic distribution are depicted in Fig. 5. As we can see, there is a general data agreement between the laboratory data and the numerical results. The total erosion of the dune is well captured, although the cavity formed right behind the dune is not present. This is a known limitation of depth-averaged models, since the phenomena involved in the creation of this depression involves vertical forces alongside turbulence effects.

4.4. Laboratory experiment with dune and slope

In this subsection, we present a different laboratory experiment with an empirical comparison. This problem is proposed in Yoshii et al. (2018), where it is labeled as C8. The configuration for this test is very similar to the previous one. Again, an uniform slope of 1/50 is set right before a 0.2-m-high sand dune. Behind the dune is a slope of 1/100. This initial condition can be seen in Fig. 6 left. As in the previous laboratory experiment, both the evolution of the free surface and velocities are readily available in Yoshii et al. (2018), and they are imposed as boundary conditions here. While all sediment parameters remain the same as in the previous experiment, the wave profile and the initial bathymetry configuration are now different. This can be seen in Fig. 6 right, that depicts the simulation at time $t = 30$ s, when the wave is close to impact the dune.

Again, we discretize the computational domain with 500 elements and we impose Dirichlet boundary conditions using the data provided in Yoshii et al. (2018). The final results, including a comparison between the laboratory experiments and the numerical solution are presented in Fig. 7. Again, we can see a outstanding data agreement between the numerical simulation and the laboratory experiment. In particular, the dune is completely destroyed by the incoming wave. Once again, this problem generates a depression in the surroundings of the dune that vertically averaged models are not able to properly simulate. However, the general morphodynamic behavior is well captured.

4.5. Impact of Tōhoku 2011 tsunami event in Crescent City harbor

This problem address morphological changes in the harbor of Crescent City (California, U.S.) during the 2011 Tōhoku tsunami event. The 2011 Tōhoku tsunami struck Japan on March 11, 2011. It was triggered by a massive undersea earthquake with a magnitude of M9.0. The epicenter was located approximately 70 km east of the Oshika Peninsula of Tōhoku and inundated over 400 km^2 of land. (see Hayes, 2011). This earthquake is among the strongest ever recorded in world history (see Satake, 2014). The tsunami waves generated by the earthquake reached astonishing heights, with some areas experiencing waves as high as 40.5 m (see Satake, 2014 or Titov, 2011).

Wilson et al. studied in Wilson et al. (2012) these morphology changes by comparing two pre- and post- event surveys conducted on February 21, 2010 and March 30, 2011 by the United States Army Corps of Engineers (USACE), the National Oceanic and Atmospheric Administration (NOAA), The U.S. Geological Survey (USGS), and several private companies and local harbor authorities.

For the boundary conditions, we use the source provided by Grilli et al. in Grilli et al. (2013) using a sequence of nested grids described by Tehranirad et al. in Tehranirad et al. (2020). A comparison of their numerical results for the source from a Deep-ocean Assessment and Reporting of Tsunamis (DART) buoy can be seen in Fig. 8. As we can see, there is a strong correlation between the numerical results and the observed data.

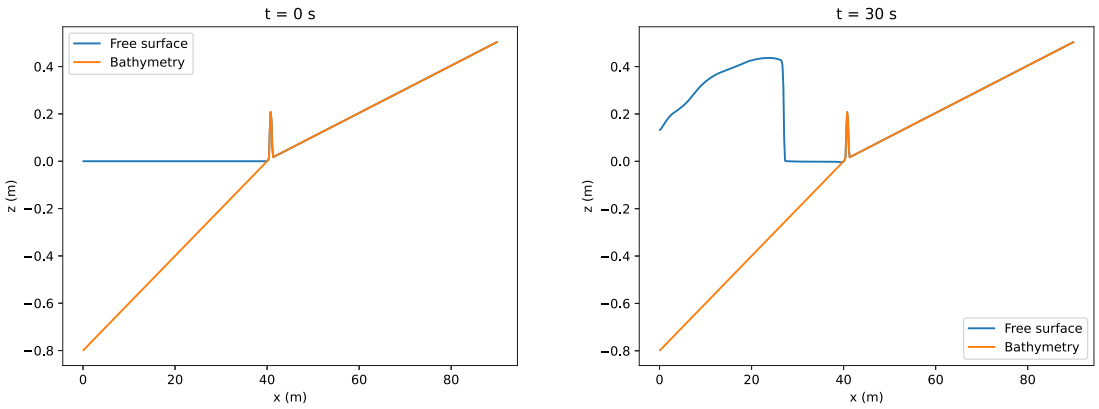

Fig. 6. Initial free surface and bathymetry (**left**) and free surface and bathymetry at time $t = 30$ s (**right**).

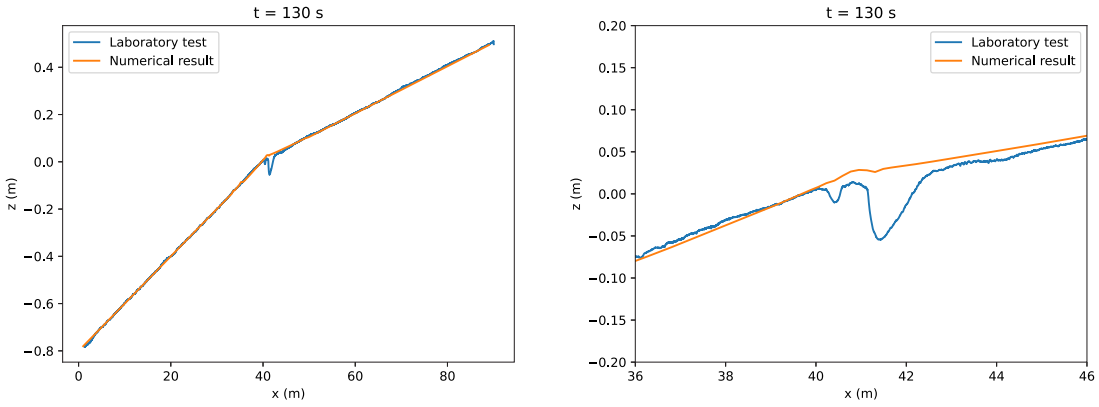

Fig. 7. Laboratory and numerical bathymetry distribution at final time $t = 130$ s (**left**) and zoom (**right**).

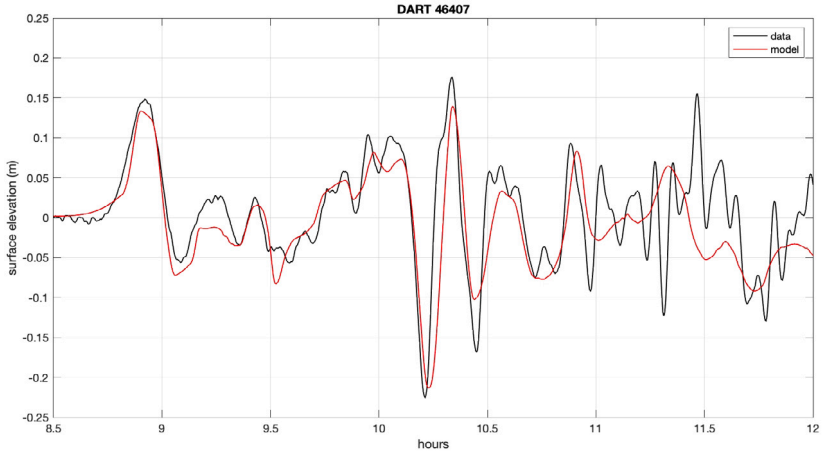

Fig. 8. Comparison of observed (black) and modeled (red) surface displacements at DART buoy 46 407 during the Tōhoku event as described in Tehranirad et al. (2020).

We discretize the domain using 501 elements in the x direction and 361 in the y direction. In this way, the discretization points coincide with those of the bathymetry source file. The sediment properties are set with the following parameters: a relative density of 2.4 with a typical grain size of 0.1 mm. The bottom friction parameter is $f = 2 \times 10^{-2}$, the porosity is set to $\phi = \frac{3}{5}$ and $\theta_{crit} = 1 \times 10^{-3}$. Furthermore, coefficients in formula (6) are adjusted with $k_1 = 40$, $m_1 = 0$, $m_2 = 3/2$ and $m_3 = 1$. These coefficients are inspired by Ashida and Michiue formula (although the coefficients are not exactly the same) and they are chosen to best fit the survey data available. As discussed in Section 2, traditional sediment transport formulations were designed for ideal tests in channels, and they do not translate directly to more complex situations. With the transport formula used here, we slightly amplify transport discharge while keeping good data agreement with existing survey data.

The results can be seen in Figs. 9 through 11. The numerical results are compared with the results from Wilson et al. in Wilson et al. (2012) in which they show the difference in bathymetry after the tsunami event. As we can see, there is a great correlation between the observed data and the numerical results. The overall morphological tendency is captured, including great erosion and deposition areas hotspots near the end of the jetty structures. This scouring is likely caused by strong currents.

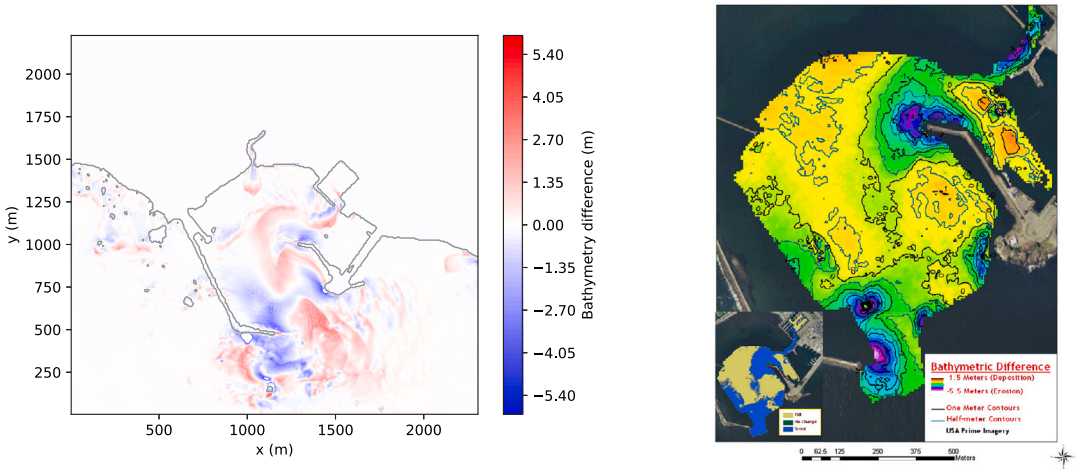

Fig. 9. Difference in bathymetry after the tsunami event. Numerical results (**left**) and Wilson et al. survey results (**right**).

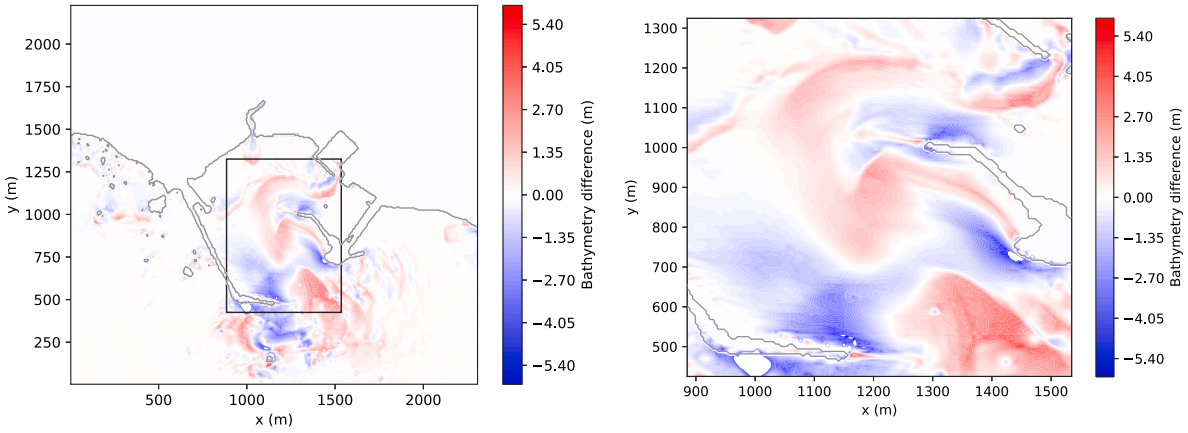

Fig. 10. Difference in bathymetry after the tsunami event. Numerical results zoom area (**left**) and zoom (**right**).

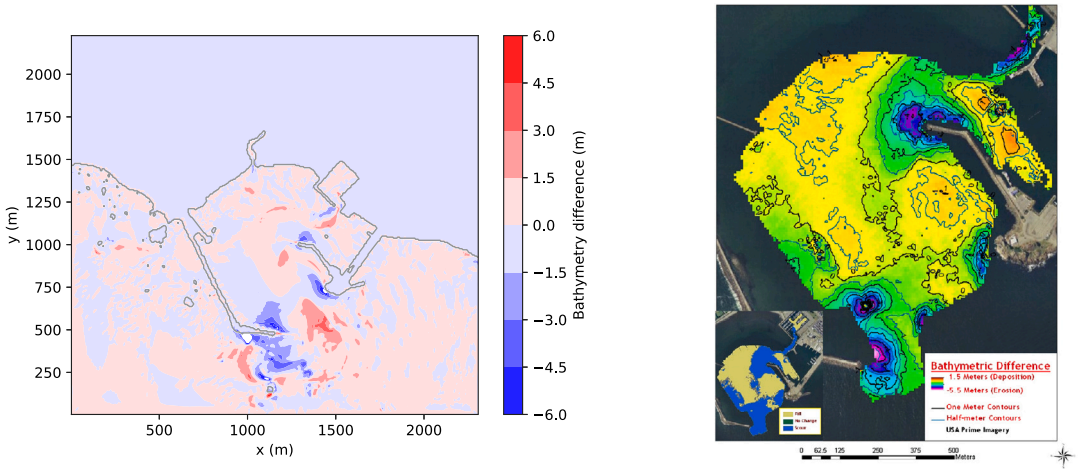

Fig. 11. Difference in bathymetry after the tsunami event. Numerical results at lower color resolution (**left**) and Wilson et al. survey results (**right**).

4.6. Impact of Tōhoku 2011 tsunami event in Hirota Bay

The final experiment concerns the impact of the 2011 Tōhoku tsunami event in Hirota Bay, in Rikuzentakata City, Japan. This problem has been thoroughly studied (see Yamashita et al., 2022 or Keiko Udo and Tanaka, 2016) due to the singular impact of the tsunami in this area, that caused great morphological changes and inundation. In particular, Yamashita et al. provide in Yamashita et al. (2022) grid data and an erodible surface map, alongside with tsunami source data. In Fig. 12 we can see the correlation between the observed tsunami elevation and the numerical results provided by Yamashita et al. in Yamashita et al. (2022). Additionally, in Fig. 13 we can see the original topology of the bay and an erodible map. Note that the

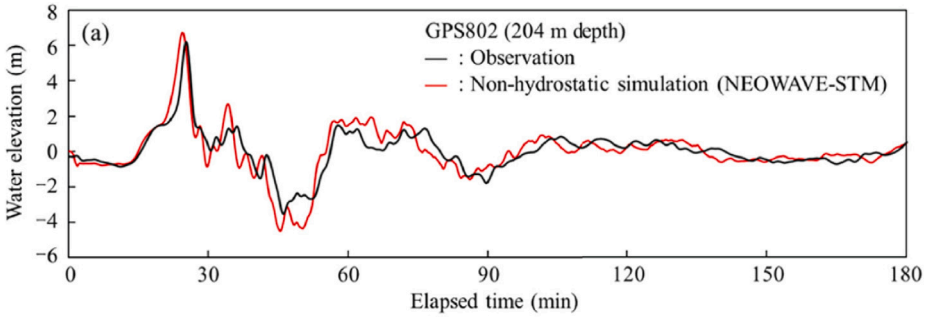

Fig. 12. Comparison between observed data and numerical results of Yamashita et al. in Yamashita et al. (2022).

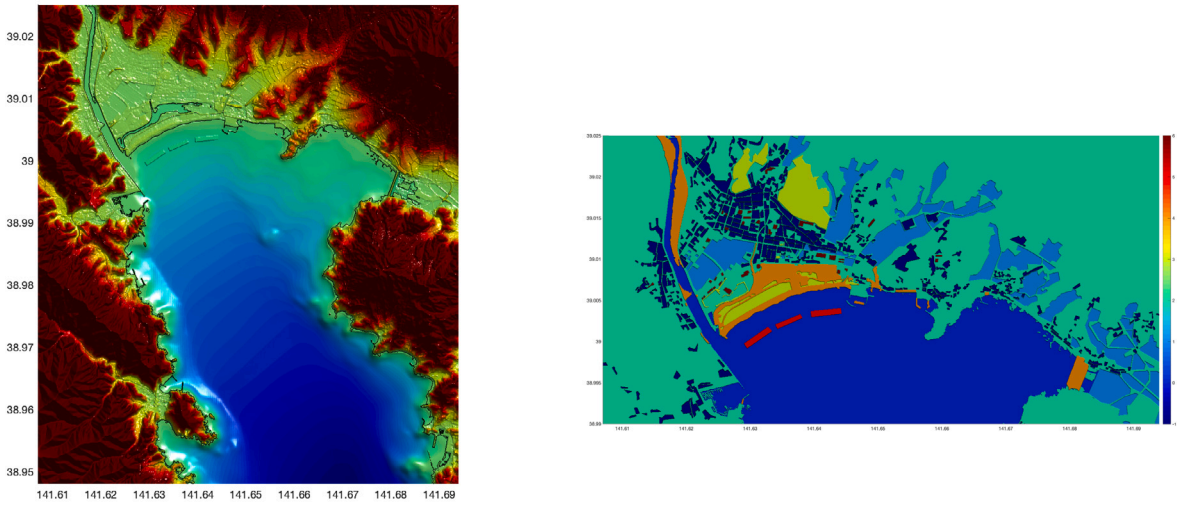

Fig. 13. Simulation grid (**left**) and erodible map (**right**) in Hirota Bay, provided by Yamashita et al. A description of the color maps can be found in Yamashita et al. (2022).

erodible map contains three non-erodible submerged breakwaters that play a significant role in the morphodynamic behavior.

The domain is discretized with 1537 elements in the x direction and 1387 elements in the y direction. Meanwhile, the sediment properties are the same as in the previous benchmark 4.5, except the friction coefficient, which is now $f = 1{\times}10^{-2}$. Additionally, the same coefficient as in the previous simulation 4.5 for formula (6) are used.

The numerical results can be seen in Fig. 14. These Figures show a comparison with a survey published in Yamashita et al. (2022). They depict the bathymetry changes before and after the tsunami event, including a zoom of the area covering the breakwaters. We have included a Figure with lower color resolution for an easier comparison with the survey data. Again, we can see an outstanding correlation between field data and the numerical results. Global tendencies, and broad erosion and deposition areas are captured. Note that the submerged breakwater structures play an important role in the global morphodynamic behavior.

5. Conclusion

We have presented a shallow-water model with bedload sediment transport and we have discussed its main properties and characteristics. We propose a numerical scheme that is second-order accurate and able to preserve lake-at-rest type of stationary solutions. This numerical discretization features a splitting technique that uses information obtained from the hydrodynamic computation to approximate the solution of the morphodynamic evolution in a weakly-coupled fashion. The numerical experiments discussed illustrate the properties of the numerical approximation, and they also provide great data agreement with both the laboratory experiments and data field surveys. The proposed model and discretization will help us to better understand sediment behavior and phenomena where these effects are relevant.

CRediT authorship contribution statement

E. Guerrero Fernández: Writing – review & editing, Writing – original draft, Visualization, Validation, Software, Methodology, Investigation, Formal analysis. **M.J. Castro Díaz:** Supervision, Formal analysis, Conceptualization. **Y. Wei:** Visualization, Resources, Project administration, Data curation. **C. Moore:** Supervision, Project administration, Funding acquisition.

Declaration of competing interest

The authors declare that they have no known competing financial interests or personal relationships that could have appeared to influence the work reported in this paper.

Data availability

Data will be made available on request.

Acknowledgments

Funding for this project was provided by the Infrastructure Investment and Jobs Act (IIJA) Provision 3 Section: Subseasonal to Annual Integrated Water Capabilities (SA), Subsection SA1.2.2. PMEL publication ID 5626. Additionally, this publication is partially funded by the Cooperative Institute for Climate, Ocean, and Ecosystem Studies (CIOCES) under NOAA Cooperative Agreement NA20OAR4320271, Contribution No. 2024-1409.

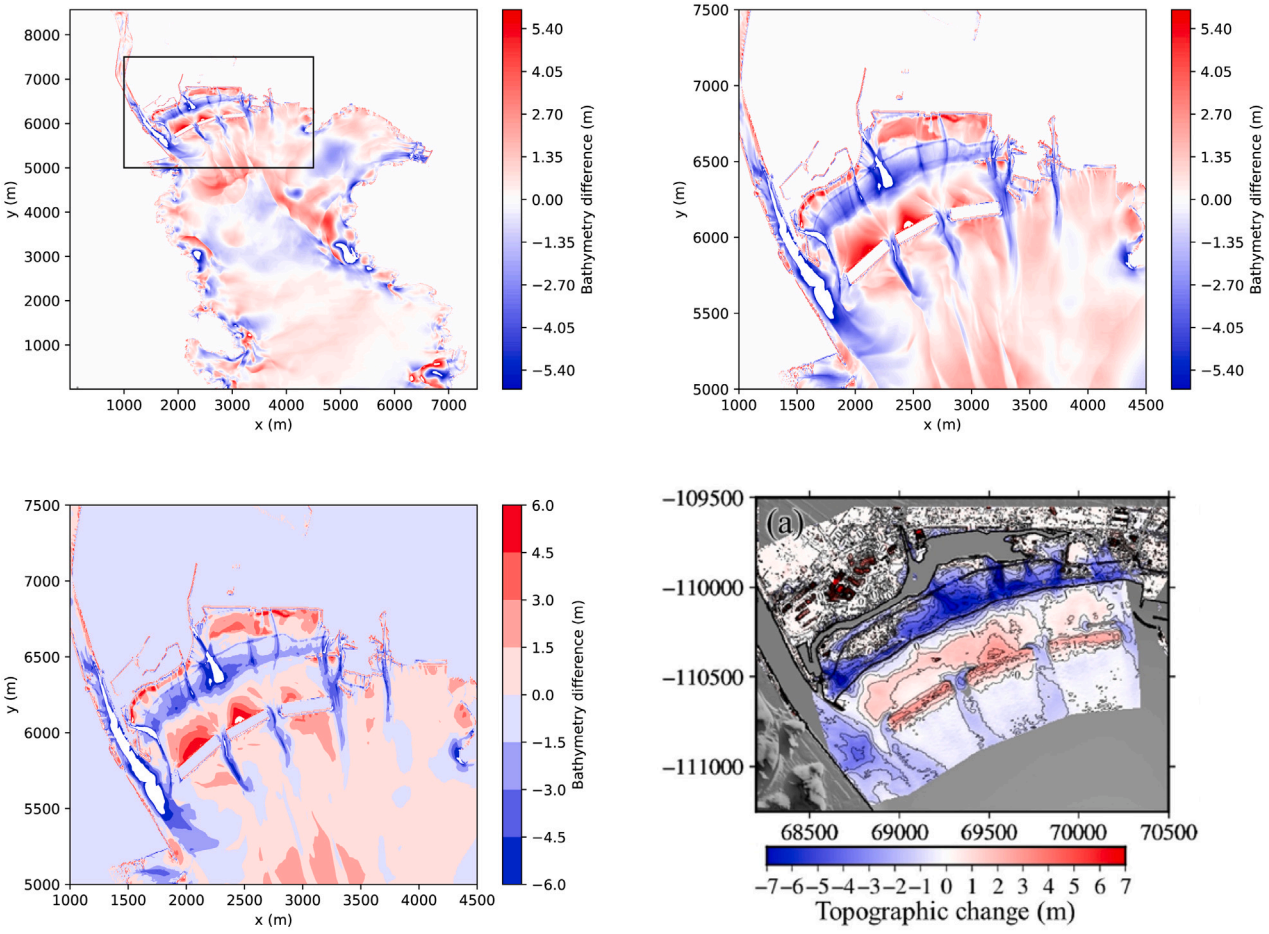

Fig. 14. Numerical results for Hirota Bay simulation. Top-left shows the general domain with the zoom area marked in a black box. Top-right depicts the zoomed area. Down-left is the same zoom area with lower color resolution while down-right shows the field survey results.

References

Ashida, K., Michiue, M., 1972. Study on hydraulic resistance and bed-load transport rate in alluvial streams. Proc. Jpn. Soc. Civ. Eng. 1972, 59–69.

De la Asunción, M., Fernández-Nieto, E., Mantas, J., Acosta, S., González-Vida, J., 2013. Efficient GPU implementation of a two waves TVD-waf method for the two-dimensional one layer shallow water system on structured meshes. Comput. & Fluids 80, 441–452, https://www.sciencedirect.com/science/article/pii/S0045793012000217, Selected contributions of the 23rd International Conference on Parallel Fluid Dynamics ParCFD2011.

Audusse, E., Bouchut, F., Bristeau, M., Klein, R., Perthame, B., 2004. A fast and stable well-balanced scheme with hydrostatic reconstruction for shallow water flows. SIAM J. Sci. Comput. 25, 2050–2065.

Bermúdez, A., López, X., Vázquez-Cendón, M., 2017. Finite volume methods for multi-component Euler equations with source terms. Comput. & Fluids 156, 113–134, https://www.sciencedirect.com/science/article/pii/S0045793017302426, Ninth International Conference on Computational Fluid Dynamics (ICCFD9).

Canestrelli, A., Siviglia, A., Dumbser, M., Toro, E., 2009. Well-balanced high-order centred schemes for non-conservative hyperbolic systems. Applications to shallow water equations with fixed and mobile bed. Adv. Water Resour. 32, 834–844, https://www.sciencedirect.com/science/article/pii/S0309170809000256.

Castro, M., Fernández-Nieto, E., 2012. A class of computationally fast first order finite volume solvers: PVM methods. SIAM J. Sci. Comput. 34.

Castro, M., Gallardo, J., Parés, C., 2006. High order finite volume schemes based on reconstruction of states for solving hyperbolic systems with nonconservative products. Applications to shallow-water systems. Math. Comp. 75, 1103–1134.

Castro, M., Morales de Luna, T., Parés, C., 2017. Chapter 6 - well-balanced schemes and path-conservative numerical methods. Handb. Numer. Methods Hyperb. Probl. 18, 131–175, https://www.sciencedirect.com/science/article/pii/S1570865916300333.

Castro, M., Pardo Milanés, A., Parés, C., 2007. Well-balanced numerical schemes based on a generalized hydrostatic reconstruction technique. Math. Models Methods Appl. Sci. 17, 2055–2113.

Castro, M., Parés, C., 2020. Well-balanced high-order finite volume methods for systems of balance laws. J. Sci. Comput. 82, 48.

Castro Díaz, M., Chacón Rebollo, T., Fernández-Nieto, E., Parés, C., 2007. On well-balanced finite volume methods for nonconservative nonhomogeneous hyperbolic systems. SIAM J. Sci. Comput. 29, 1093–1126. http://dx.doi.org/10.1137/040607642.

Castro Díaz, M., Fernández-Nieto, E., Ferreiro, A., 2008. Sediment transport models in Shallow water equations and numerical approach by high order finite volume methods. Comput. & Fluids 37, 299–316, http://www.sciencedirect.com/science/article/B6V26-4PSK8R5-1/2/9043410cc90abc43b410c70660a4efd6.

Castro Díaz, M., Fernández-Nieto, E., Ferreiro, A., Parés, C., 2009. Two-dimensional sediment transport models in shallow water equations. a second order finite volume approach on unstructured meshes. Comput. Methods Appl. Mech. Engrg. 198, 2520–2538, https://www.sciencedirect.com/science/article/pii/S0045782509001169.

Cordier, S., Le, M., Morales de Luna, T., 2011. Bedload transport in shallow water models: Why splitting (may) fail, how hyperbolicity (can) help. Adv. Water Resour. 34, 980–989, https://www.sciencedirect.com/science/article/pii/S0309170811000935.

Dal Maso, G., LeFloch, G.P., Murat, F., 1995. Definition and weak stability of nonconservative products. Journal de Mathématiques Pures Et Appliquées. Neuvième Série 74.

Darcy, H., 1857. Recherches expérimentales relatives au mouvement de l'eau dans les tuyaux. Impr. Imp. https://books.google.com/books?id=s88WAAAAQAAJ.

De St Venant, B., 1871. Théorie du mouvement non permanent des eaux, avec application aux crues des rivières et à l'introduction des marées dans leur lit. Acad. Sci. Comptes Redus 73, 148–154.

Einstein, H., 1950. The Bed-Load Function for Sediment Transportation in Open Channel Flows. United States Department of Agriculture, Economic Research Service, https://ideas.repec.org/p/ags/uerstb/156389.html.

Exner, F., 1925. Über die Wechselwirkung zwischen Wasser und Geschiebe in Flüssen: Gedr. mit Unterstütz aus d. Jerome u. Margaret Stonborough-Fonds, https://books.google.com/books?id=7bjqZwEACAAJ,

Fernández, E., Díaz, M., Dumbser, M., Luna, T., 2021. An arbitrary high order well-balanced ADER-DG numerical scheme for the multilayer shallow-water model with variable density. J. Sci. Comput. 90, 52. http://dx.doi.org/10.1007/s10915-021-01734-2.

Gottlieb, S., Shu, C., 1996. Total variation diminishing Runge–Kutta schemes. Math. Comp. 67.

Grass, A., 1981. Sediment Transport By Waves and Currents. University College, London, Department of Civil Engineering, https://books.google.es/books?id=YU0QAQAAIAAJ.

Grilli, S., Harris, J., Tajalli Bakhsh, T., Masterlark, T., Kyriakopoulos, C., Kirby, J., Shi, F., 2013. Numerical simulation of the 2011 tohoku Tsunami based on a new transient FEM co-seismic source: Comparison to far- and near-field observations. Pure Appl. Geophys. 170, 1333–1359. http://dx.doi.org/10.1007/s00024-012-0528.

Guerrero Fernández, E., Castro-Díaz, M., Luna, T., 2020. A second-order well-balanced finite volume scheme for the multilayer shallow water model with variable density. Mathematics 8, 848.

Guerrero Fernández, E., Escalante, C., Castro Díaz, M., 2022. Well-balanced high-order discontinuous Galerkin methods for systems of balance laws. Mathematics 10, https://www.mdpi.com/2227-7390/10/1/15.

Hager, W., Boes, R., 2018. Eugen Meyer-Peter and the MPM sediment transport formula. J. Hydraul. Eng. 144, 02518001, https://ascelibrary.org/doi/abs/10.1061/.

Hayes, G., 2011. Rapid source characterization of the 2011 Mw 9.0 off the Pacific coast of Tohoku earthquake. Earth Planets and Space 63, 529–534. http://dx.doi.org/10.5047/eps.2011.05.012.

Julien, P., 2010. Erosion and Sedimentation. Cambridge University Press.

Kalinske, A., 1942. Criteria for determining sand-transport by surface-creep and saltation. Trans. Am. Geophys. Union 23, 639–643.

Kalinske, A., 1947. Movement of sediment as bed load in rivers. EOS Trans. Am. Geophys. Union 28, 615–620, https://agupubs.onlinelibrary.wiley.com/doi/abs/10.1029/TR028i004p00615.

Keiko Udo, Y., Tanaka, H., 2016. Coastal morphology change before and after 2011 off the Pacific coast of Tohoku earthquake tsunami at Rikuzen-Takata Coast. Coast. Eng. J. 58, 1640016-1-1640016-16. http://dx.doi.org/10.1142/S0578563416400167.

Kurkina, O., Talipova, T., Pelinovsky, E., Soomere, T., 2011. Mapping the internal wave field in the baltic sea in the context of sediment transport in shallow water. J. Coast. Res. 2042–2047, http://www.jstor.org/stable/26482535.

Leer, B., 1979. Towards the ultimate conservative difference scheme. V. A second-order sequel to Godunov's method. J. Comput. Phys. 32, 101–136.

Li, S., Duffy, C., 2011. Fully coupled approach to modeling shallow water flow, sediment transport, and bed evolution in rivers. Water Resour. Res. 47, https://agupubs.onlinelibrary.wiley.com/doi/abs/10.1029/2010WR009751.

Luque, R. Fernandez, Beek, R. Van, 1976. Erosion and transport of bed-load sediment. J. Hydraul. Res. 14, 127–144.

Manning, R., Griffith, J., Pigot, T., Vernon-Harcourt, L., 1890. On the flow of water in open channels and pipes.

Meyer-Peter, E., Müller, R., 1948. Formulas for bed-load transport. In: IAHSR 2nd Meeting. Stockholm, Appendix 2.

Nielsen, P., 1992. Coastal Bottom Boundary Layers and Sediment Transport. WORLD SCIENTIFIC, https://www.worldscientific.com/doi/abs/10.1142/1269.

Parés, C., 2006. Numerical methods for nonconservative hyperbolic systems: a theoretical framework. SIAM J. Numer. Anal. 44, 300–321.

Ribberink, J., 1987. Mathematical Modelling of One-Dimensional Morphological Changes in Rivers with Non-Uniform Sediment. Citeseer.

Rijn, L., 1984. Sediment transport, part I: Bed load transport. J. Hydraul. Eng. 110, 1431–1456, https://ascelibrary.org/doi/abs/10.1061/.

Rijn, L., 1984a. Sediment transport, Part II: Suspended load transport. J. Hydraul. Eng. 110, 1613–1641, https://ascelibrary.org/doi/abs/10.1061/.

Rijn, L., 1984b. Sediment transport, Part III: Bed forms and alluvial roughness. J. Hydraul. Eng. 110, 1733–1754, https://ascelibrary.org/doi/abs/10.1061/.

Satake, K., 2014. The 2011 tohoku, Japan, earthquake and tsunami. Extrem. Nat. Hazards Disaster Risks Soc. Implic. 310–321.

Tang, H., Weiss, R., 2016. GeoClaw-STRICHE: A coupled model for sediment transport In Coastal hazard events. arXiv https://arxiv.org/abs/1609.04791.

Teeter, A., Johnson, B., Berger, C., Stelling, G., Scheffner, N., Garcia, M., Parchure, T., 2001. Hydrodynamic and sediment transport modeling with emphasis on shallow-water, vegetated areas (lakes, reservoirs, estuaries and lagoons). Hydrobiologia 444, 1–23. http://dx.doi.org/10.1023/A:1017524430610.

Tehranirad, B., Kirby, J., Shi, F., 2020. A numerical model for Tsunami-induced morphology change. Pure Appl. Geophys. 178, 5031–5059, https://api.semanticscholar.org/CorpusID:226294752.

Titov, V., 2011. Tohoku-Japan tsunami: lessons from forecast assessment. In: Proceedings of the 2012 Joint International Conference on Human-Centered Computer Environments. Vol. 9, pp. 9–100. http://dx.doi.org/10.1145/2160749.2160771, March 11, 2011.

Toro, E., 2013. Riemann Solvers and Numerical Methods for Fluid Dynamics: A Practical Introduction, third ed. Springer Science & Business Media.

Wilson, R., Davenport, C., Jaffe, B., 2012. Sediment scour and deposition within harbors in California (USA), caused by the march 11 2011 Tohoku-oki tsunami. Sediment. Geol. 282, 228–240, https://www.sciencedirect.com/science/article/pii/S0037073812001595, The 2011 Tohoku-oki tsunami.

Yalin, M., Karahan, E., 1979. Inception of sediment transport. J. Hydraul. Eng. 105, 1433–1443.

Yamashita, K., Yamazaki, Y., Bai, Y., Takahashi, T., Imamura, F., Cheung, K., 2022. Modeling of sediment transport in rapidly-varying flow for coastal morphological changes caused by tsunamis. Mar. Geol. 449, 106823, https://www.sciencedirect.com/science/article/pii/S0025322722000949.

Yoshii, T., Tanaka, S., Matsuyama, M., 2017. Tsunami deposits in a super-large wave flume. Mar. Geol. 391, 98–107, https://www.sciencedirect.com/science/article/pii/S002532271730244X.

Yoshii, T., Tanaka, S., Matsuyama, M. Tsunami, 2018. Tsunami inundation, sediment transport, and deposition process of tsunami deposits on coastal lowland inferred from the tsunami sand transport laboratory experiment (TSTLE). Mar. Geol. 400, 107–118, https://www.sciencedirect.com/science/article/pii/S0025322717304632.

Zee, C., Zee, R., 2017. Formulas for the transportation of bed load. J. Hydraul. Eng. 143, 04016101, https://ascelibrary.org/doi/abs/10.1061/.